Short Communication | **Open Access**

Artificial Intelligence Surgery

Scariah *et al*. *Art Int Surg*. 2026;6:395-416 **DOI:**10.20517/ais.2026.22

Developing an algorithm for virtual fracture reduction (VFR) of mandibular fractures using CT scans: a preliminary technical study

Ajin Scariah[1,#], Leonard Knoedler[2,#], Thomas Koett[1], Adem Aksu[1], Thomas Potrusil[3], Tobias Niederegger[2], Murtaja Satea[4,5], Jonas Fischer[6], Max Heiland[2], Jan Oliver Voss[2]

Keywords:
Virtual fracture reduction, VFR, mandibular fractures, facial fractures, CT scans

Citation: Scariah A, Knoedler L, Koett T, Aksu A, Potrusil T, Niederegger T, Satea M, Fischer J, Heiland M, Voss JO. Developing an algorithm for virtual fracture reduction (VFR) of mandibular fractures using CT scans: a preliminary technical study. *Art Int Surg*. 2026;6:395-416. https://dx.doi.org/10.20517/ais.2026.22

Received: 3 Apr 2026
First Decision: 11 Jun 2026
Revised: 4 Aug 2026
Accepted: 14 Aug 2026
Published: 25 Aug 2026

Academic Editor: Eyad Elyan
Copy Editor: Tong Wang
Production Editor: Tong Wang

Check for updates

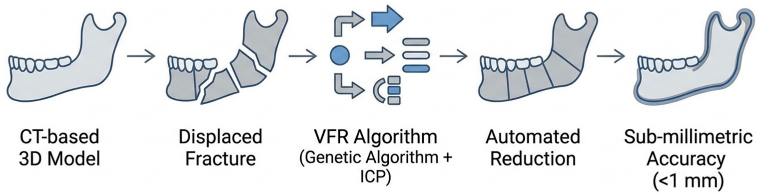

Abstract

Aim: Mandibular fractures are common and challenging to reduce accurately, particularly in multi-fragment or edentulous settings. Virtual fracture reduction (VFR) could standardize preoperative planning and provide millimetric targets for open reduction and internal fixation but remains limited by manual workflows and variable imaging quality.

Methods: We developed a two-stage VFR algorithm using computed tomography (CT)-derived 3D models. Coarse alignment was achieved via a genetic optimization algorithm, followed by fine alignment with the Iterative Closest Point (ICP) algorithm. A weighted objective function optimized (i) condylar positioning, (ii) dental occlusion, and (iii) fracture gap minimization. We tuned weights over 14 experiments and optimized 6 pose parameters per segment with a Genetic Algorithm. Accuracy was evaluated on a synthetic

[1]KLS Martin SE & Co. KG, Mühlheim an der Donau 78532, Germany.
[2]Charité - Universitätsmedizin Berlin, Corporate member of Freie Universität Berlin and Humboldt-Universität zu Berlin, Department of Oral and Maxillofacial Surgery, Berlin 13353, Germany.
[3]CADS GmbH, Perg 4320, Austria.
[4]Department of Surgery, University of Warith Al-Anbiyaa, College of Medicine, Karbala 56001, Iraq.
[5]Division of Plastic Surgery, Microsurgery and Regenerative Medicine Laboratory, University of Wisconsin School of Medicine and Public Health, Madison, WI 53705, USA.
[6]Department of Engineering and Natural Sciences, Merseburg University of Applied Sciences, Merseburg 06217, Germany.
[#]These authors contributed equally to this work.

Correspondence to: Dr. Murtaja Satea, Division of Plastic Surgery, Microsurgery and Regenerative Medicine Laboratory, University of Wisconsin School of Medicine and Public Health, Madison, WI 53705, USA. E-mail: murtaja.satea@gmail.com; Dr. Jan Oliver Voss, Charité - Universitätsmedizin Berlin, Corporate member of Freie Universität Berlin and Humboldt-Universität zu Berlin, Department of Oral and Maxillofacial Surgery, Berlin 13353, Germany. E-mail: jan.voss@charite.de

fracture model and applied to three clinical cases. Outcomes included surface-distance maps, occlusal landmark deviation, interfragmentary gaps, and overlap volume and direct contact area.

Results: On the synthetic model, maximum surface deviation was 1.58 mm, with fracture-surface errors predominantly < 1 mm. Occlusal reconstruction reproduced molar relationships within 0.07-0.15 mm of the pre-fracture model. In three clinical cases (simple and comminuted patterns), mean interfragmentary gaps were 0.22-0.70 mm, overlap volumes ranged from 28.54 to 119.26 mm^3, and direct contact areas spanned 216.00-533.17 mm^2, indicating minimal interpenetration and substantial bone-to-bone fit. The pipeline demonstrated stable convergence and reproducible alignment without intraoperative data.

Conclusion: These preliminary technical findings support the proposed VFR algorithm as a practical proof-of-concept adjunct to trauma planning. Larger multicenter clinical validations with statistical analyses and functional endpoints are warranted to validate its clinical impact and scalability.

BACKGROUND

Each year, around 11 million new facial fractures are recorded globally, of which more than 25% involve the mandible[1,2]. Frequent injury patterns include physical violence, traffic accidents, sports injuries, and falls, commonly affecting middle-aged male individuals[3]. Paramedian fractures comprise 25%-35%, angle fractures 20%-30%, and condylar fractures 15%-25%, whereas ramus and coronoid injuries account for only ~2%-3%[4-6]. Interestingly, nearly half of the patients present with multiple fractures of the mandible[7,8]. Collectively, mandibular fractures represent a persistent challenge for patients and providers, with rising incidence and increasing cost burden[2,9].

There are different conservative and surgical treatments for mandibular fractures. Conservative therapies, involving various maxillomandibular fixation techniques, are often performed for minimally displaced fractures, especially in pediatric or edentulous patients[10,11]. Open reduction and internal fixation (ORIF) with mini-plates is considered the current standard surgical approach, accounting for ~75% of surgical mandibular fracture repairs[12]. Conversely, comminuted, atrophic, or edentulous sites may warrant the use of larger reconstruction plates[13]. Between 5% and 15% of patients report postoperative complications, of which wound infections and non-union are the most common[14-16].

To further improve postoperative outcomes, virtual surgical planning (VSP) has recently gained interest in maxillofacial surgery, particularly for elective procedures such as tumor resection, reconstruction, and orthognathic surgery[17-20]. While VSP enhances surgical accuracy, efficiency, and individualization, its use in trauma care remains limited due to the time-intensive preoperative planning process, which may delay treatment. However, virtual fracture reduction (VFR) as part of VSP holds promise for improving the management of mandibular fractures. This umbrella term describes a digital workflow, ranging from preoperative computed tomography (CT)-based segmentation and 3D fragment identification to computer-guided fracture repositioning to help reconstruct pre-injury anatomy[21]. VFR also serves as a data source for computer-aided design and computer-aided manufacturing (CAD/CAM)-fabricated guides or pre-bent plates[22]. VFR has been demonstrated to improve the accuracy of mandibular reconstructions and postoperative occlusion compared with conventional free-hand methods[23,24], reduce operative times[25], and provide high inter-operator reproducibility, with root-mean-square deviations of < 2 mm from reference geometry[26].

VFR primarily involves matching and registering displaced fragments to their original positions. Manual virtual reduction is commonly used in clinical practice where surgeons interact with three-dimensional models of fractured bones using mouse-and-screen interfaces, haptic devices, or virtual reality (VR) environments[27-29]. However, manual virtual reduction methods are time-consuming, subjective, and show poor inter-rater reliability, limiting their widespread clinical adoption and efficiency, especially in the treatment of combined/multi-fragment fractures[30].

Automated techniques reduce human intervention by leveraging computational algorithms. The Iterative Closest Point (ICP) approach leverages the unaffected contralateral side of the bone to serve as an anatomical template, and the fractured bone fragments are aligned to this reference model by minimizing the distances between corresponding surface points[31-33]. Statistical Shape Models (SSMs) capture population-level anatomical variations to reconstruct patient-specific geometries. Fragments are registered to an adaptive SSM template that accounts for shape and pose variability[34,35]. Landmark-based rigid registration identifies at least three corresponding landmark pairs on each side of the fracture gap to compute point-based alignment for virtual reduction. This method was applied to mandibular fractures. To preserve anatomical integrity, a distance constraint maintains condylar positioning during reduction[18].

However, workflow bottlenecks and feasibility issues (e.g., manual repositioning of fracture fragments) in time-critical mandibular trauma cases still hinder widespread clinical adoption of VFR[26,36]. To overcome these hurdles, we developed a novel algorithm to automatically reposition mandibular bone fragments back to their original anatomical location. The algorithm integrates a two-stage approach combining optimization techniques for initial coarse alignment and the ICP algorithm for precise final alignment[37]. This methodology was designed to optimize three critical factors: (i) accurate positioning of the mandibular condyle within the mandibular fossa to ensure temporomandibular joint (TMJ) stability and mobility, (ii) achievement of satisfactory dental occlusion for functional tooth alignment, and (iii) minimization of interfragmentary gaps to enhance bone healing. An overview of the algorithm is detailed in Figure 1. Designed as part of a software tool to support rapid and reliable planning in urgent trauma care, our algorithm represents a key step toward a streamlined digitalized workflow for patients with mandibular fractures.

MATERIALS AND METHODS

Ethical approval

Approval for this research was granted by the Ethics Committee at Charité - Universitätsmedizin Berlin (EA2/214/24). Anonymized preoperative CT scans were retrospectively collected at the Department of Oral and Maxillofacial Surgery, Charité-Universitätsmedizin Berlin, Campus Virchow-Klinikum. The scans were taken as part of routine preoperative assessments in patients presenting with mandibular fractures. Image acquisition followed a standardized clinical protocol and was performed on General Electric CT systems (LightSpeed VCT and Pro 16, Fairfield, CT, USA). Digital Imaging and Communications in Medicine (DICOM) data sets of CT scans from 88 individuals were analyzed and served as the basis for VFR algorithm development. Scans were acquired with a slice thickness of 0.625 mm and reconstructed using a bone kernel with a reconstruction interval of 0.5-1.0 mm. Acquisition parameters included 120 kVp, automated mA modulation, a matrix size of 512 × 512, and a field of view (FOV) adapted to the craniofacial region (~180-220 mm). All scans were performed without contrast enhancement and in axial acquisition mode.

Segmentation and 3D model reconstruction

Segmentation of the mandibular bone and associated fracture fragments was performed using Materialise Mimics 23.0 (Materialise NV, Leuven, Belgium). The software provides intensity-based segmentation directly from DICOM-formatted CT data using predefined Hounsfield unit (HU) thresholds for bone tissue. An

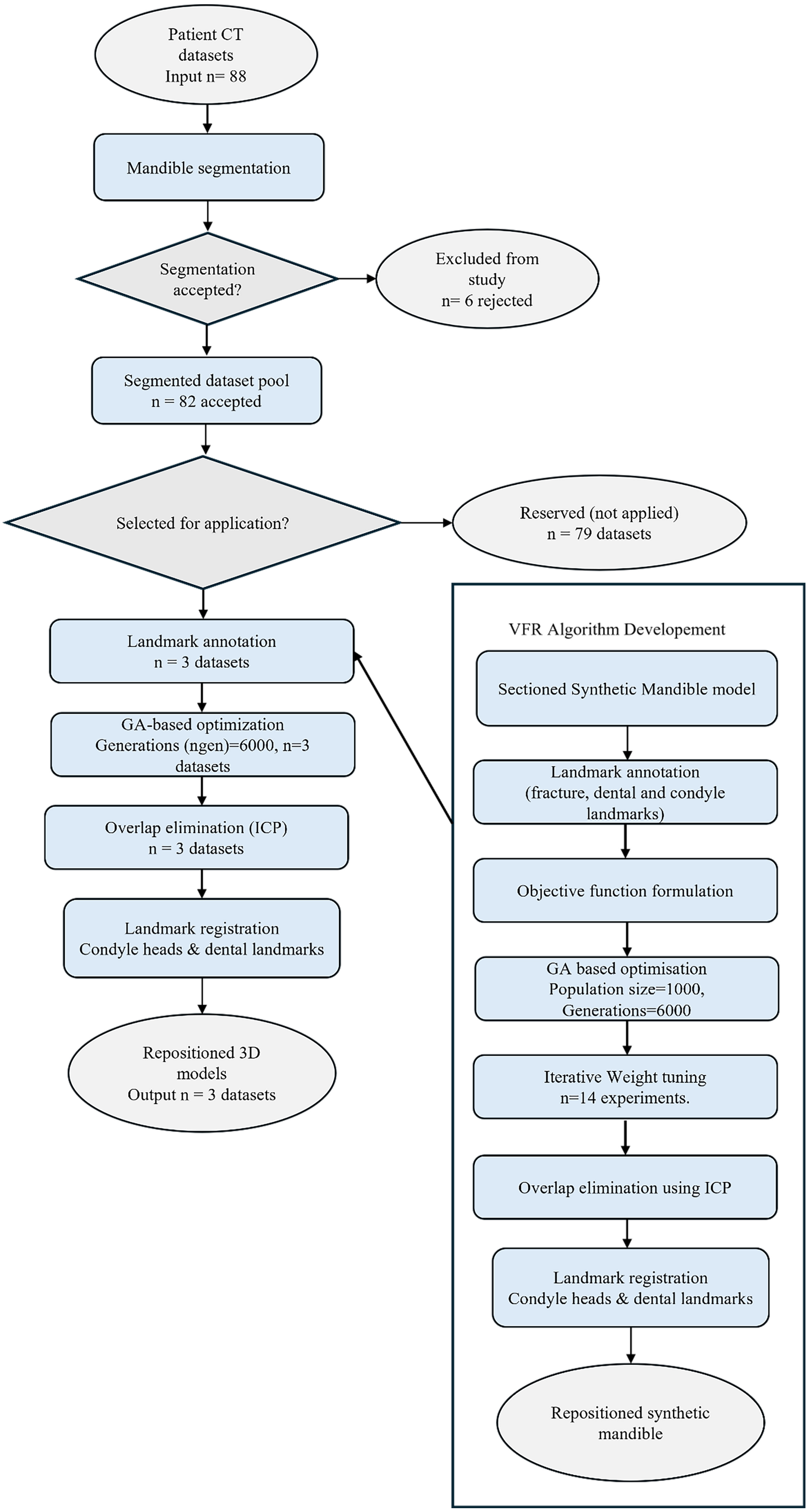

Figure 1. Overview of the VFR algorithm: (left) clinical application pipeline; (right) offline development and parameter-tuning pipeline using a synthetic mandible model. VFR: Virtual fracture reduction.

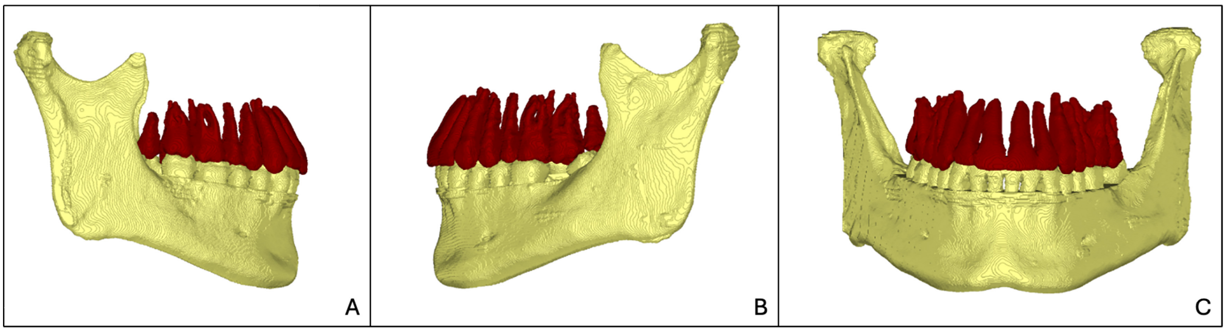

Figure 2. Virtual synthetic mandible model. (A) Right lateral view of the mandible with dentition; (B) Left lateral view of the mandible with dentition; (C) Frontal view showing the complete mandibular arch and dentition.

automatic thresholding procedure was applied to isolate cortical and trabecular bone structures, typically within the HU range of 300-2,000. This mask was refined using region-growing and morphological editing tools to separate individual fracture fragments and eliminate noise from surrounding soft tissues. After segmentation, the resulting masks were converted into 3D surface models. Each fragment was exported in stereolithography (STL) format for further processing and algorithmic repositioning.

Synthetic mandible model

The algorithm was initially developed and tested using a synthetic mandibular model based on two anonymized full-body CT scans. Both volumes were manually cropped to the head and neck region and forwarded to our artificial intelligence (AI)-segmentation pipeline for automatic annotation of relevant skull structures[38]. The mandible mean-shape model, including teeth, was created by averaging vertex coordinates from their meshes while retaining the main mesh topology. The resulting model preserves the original vertex connectivity and topology, representing an averaged mandible geometry without any individual anatomical information [Figure 2].

To simulate a fracture scenario, the virtual mandible was sectioned with random rotational displacements [Figure 3]. This synthetic fracture model provided a controlled environment for iterative parameter tuning, performance evaluation, and optimization of the VFR algorithm.

Anatomical landmarks

A dedicated in-house-developed Landmark Editor was used, with Qt Quick/QML for the graphical user interface and Visualization Toolkit (VTK) for interactive three-dimensional visualization. Landmarks were manually placed on STL surface models and could subsequently be selected, renamed, renumbered, or deleted. Landmark coordinates were exported for each surface model as three-dimensional (x), (y), and (z) values with four decimal places in a JSON-based file for further processing.

The algorithm utilizes three types of anatomical landmarks to guide fracture repositioning: (i) Dental Landmarks: These are specific reference points on the teeth critical for achieving proper occlusion. Key landmarks include the mesiopalatinal cusp of the maxillary molars, the central fossa of the mandibular molars, and the midpoints of the maxillary and mandibular arches (MidU and MidS, respectively), which ensure symmetry and functional harmony in dental articulation [Figures 4 and 5]; (ii) Fracture Landmarks: These are defined points characterizing the sectional features of fractured surfaces. Each landmark on one

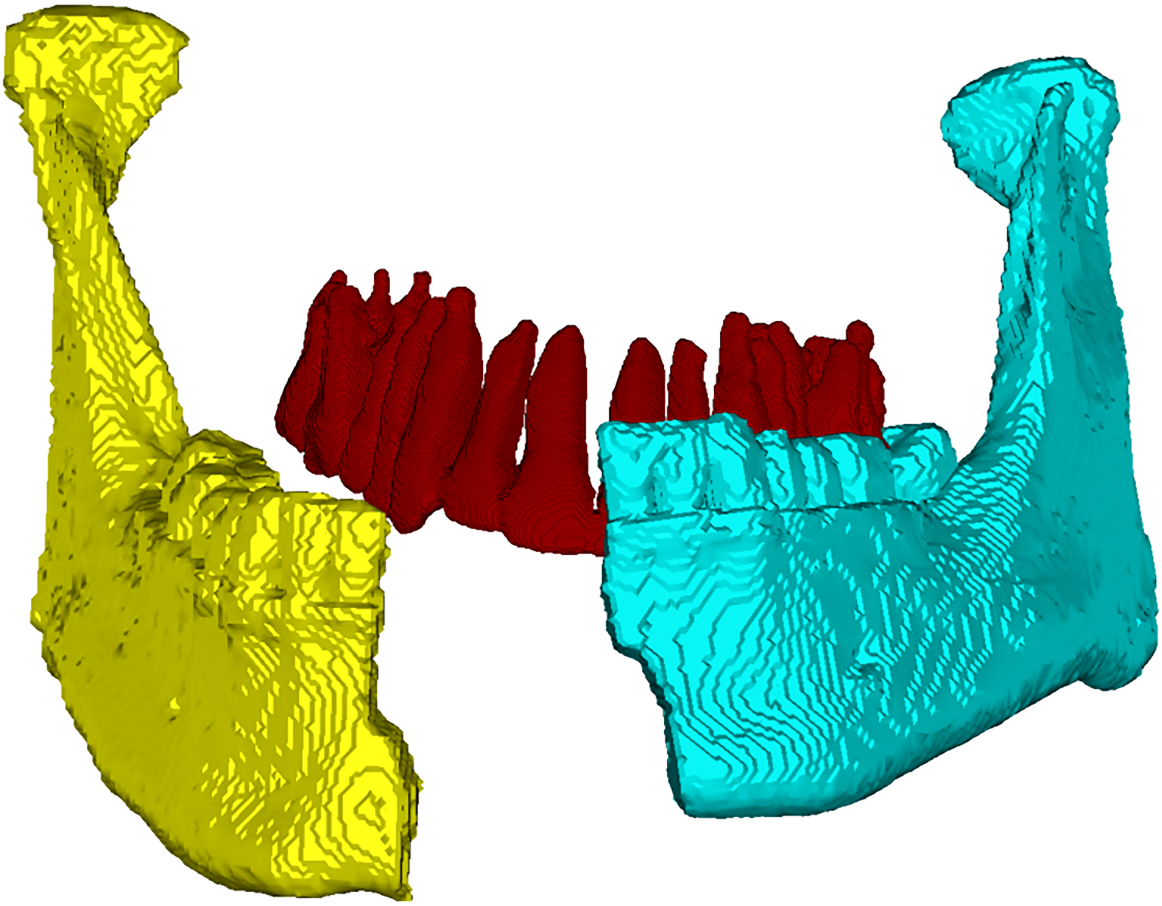

Figure 3. Simulated fracture on synthetic mandible.

fragment corresponds to a counterpart on the opposing fragment, enabling precise alignment and analysis of fracture patterns [Figure 6]; (iii) Condylar Head Landmarks: These are anatomical reference points on the mandibular condyle heads (CHL, CHLT for the left side; CHR, CHRT for the right side), critical for positioning the condyle within the mandibular fossa to ensure TMJ functionality [Figure 7].

Objective function and optimization

The algorithm employs a weighted objective function to optimize the alignment of mandibular segments, incorporating multiple constraints to address dental occlusion, condylar positioning, and fracture gap minimization:

$$\begin{aligned}&\mathrm{Min}\left(w1\frac{\sum\|LS1-LUS1\|^2}{M}+w2\frac{\sum\|LS2-LUS2\|^2}{N}+w3\|\,\mathrm{MidS}[:,0]-\mathrm{MidU}[:,0]\|^2\right.\\&+w4\|CHL-CHLT\|^2+w5\|CHR-CHRT\|^2+w6\frac{\sum\|JS1-JS2S1\|^2}{K}\\&+w7\textstyle\sum_{i=1}(\mathrm{LS\,1}[:,1]<\mathrm{LUS\,1}[:,1])+w8\sum(\mathrm{LS\,2}[:,1]<\mathrm{LUS\,2}[:,1])\\&\left.+w9\textstyle\sum_{z}(JS1[:,0]<JS2S1[:,0])\right)\end{aligned}$$

The objective function is defined as a weighted sum of nine terms: (i) Terms 1-3 align mandibular and maxillary dental landmarks (LS1, LS2, LUS1, LUS2, MidS, MidU) to ensure proper occlusion; (ii) Terms 4-5 regulate condylar head positioning (CHL, CHLT, CHR, CHRT) for TMJ articulation; (iii) Term 6 minimizes

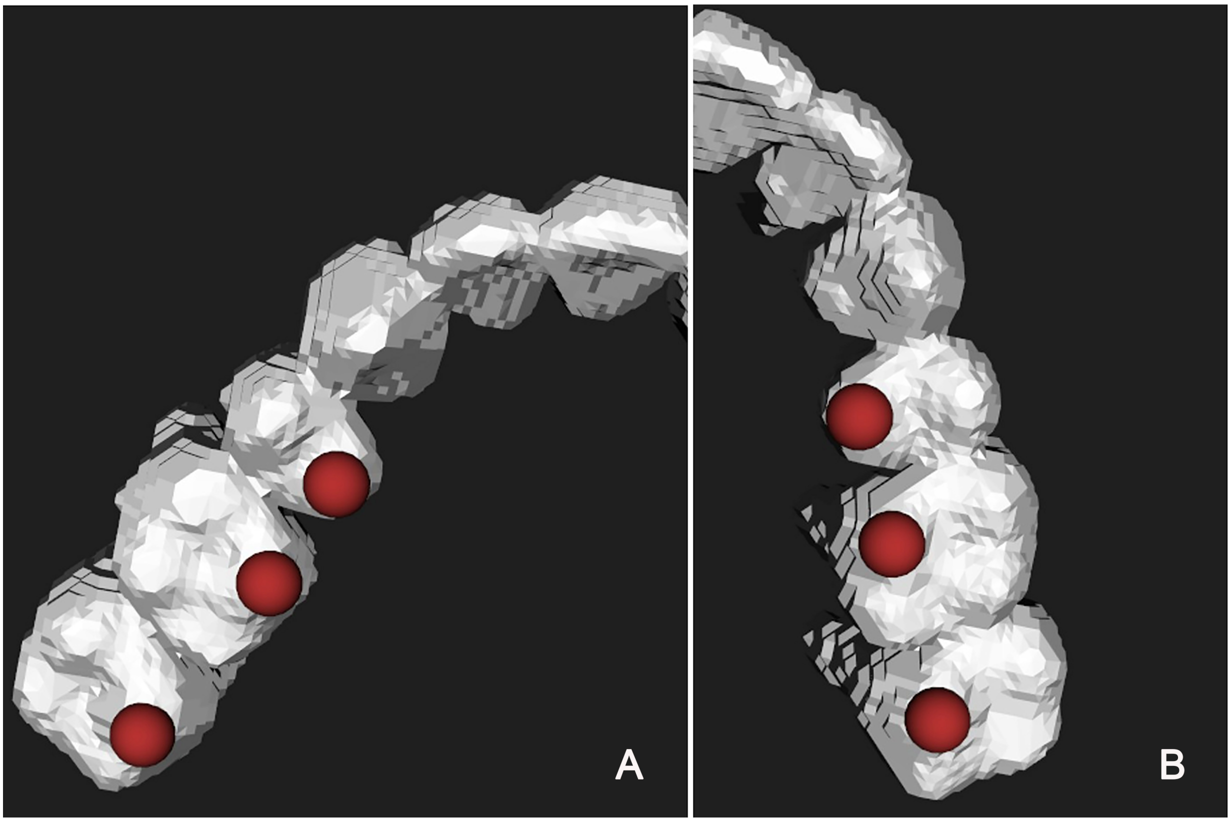

Figure 4. Maxillary dentition with landmark positioning. (A) Upper right dentition with landmarks indicated by red dots; (B) Upper left dentition with landmarks indicated by red dots.

the gap between fracture landmarks (JS1, JS2S1) to enhance bone healing; and (iv) Terms 7-9 prevent interpenetration and volume overlaps between 3D segments to ensure anatomical feasibility. The objective function quantifies alignment error as the weighted sum of squared differences between transformed and target landmark positions, with weights reflecting clinical priorities. A genetic algorithm (GA) facilitated by the DEAP library framework was employed to optimize the transformation parameters (rotation and translation) for each mandibular segment, with each GA individual encoding 12 parameters: six for rotation (three angles per segment, constrained to ± 0.349 radians) and six for translation (three values per segment, constrained to ± 10 mm)[39].

The GA was configured with the following parameters: (i) Population size of 1,000 individuals, initialized with zero parameters - this neutral starting point allows the algorithm to systematically explore the solution space and identify optimal transformations without an initial bias; (ii) Generations set to 6,000 iterations; (iii) Genetic operators including crossover using blend crossover (cxBlend) with a blending factor (alpha) of 0.5 and a crossover probability (cxpb) of 0.9, mutation using Gaussian mutation (mutGaussian) with a mutation strength (sigma) of 0.2 and an individual mutation probability (indpb) of 0.2, and selection using tournament selection with a tournament size of 3. Fitness was evaluated based on the total alignment error, and statistical metrics (average, standard deviation, minimum, and maximum fitness) were recorded per generation to monitor convergence. The optimal transformation parameters were then used to construct 4 × 4 transformation matrices, which were applied to the 3D mesh representations for precise segment realignment.

To ensure reproducibility, a fixed random seed (seed = 42) was set for both NumPy and Python's random module prior to population initialization. Given identical input data and a fixed seed, the GA's stochastic operators (Gaussian mutation, tournament selection) produce deterministic and reproducible results across repeated executions.

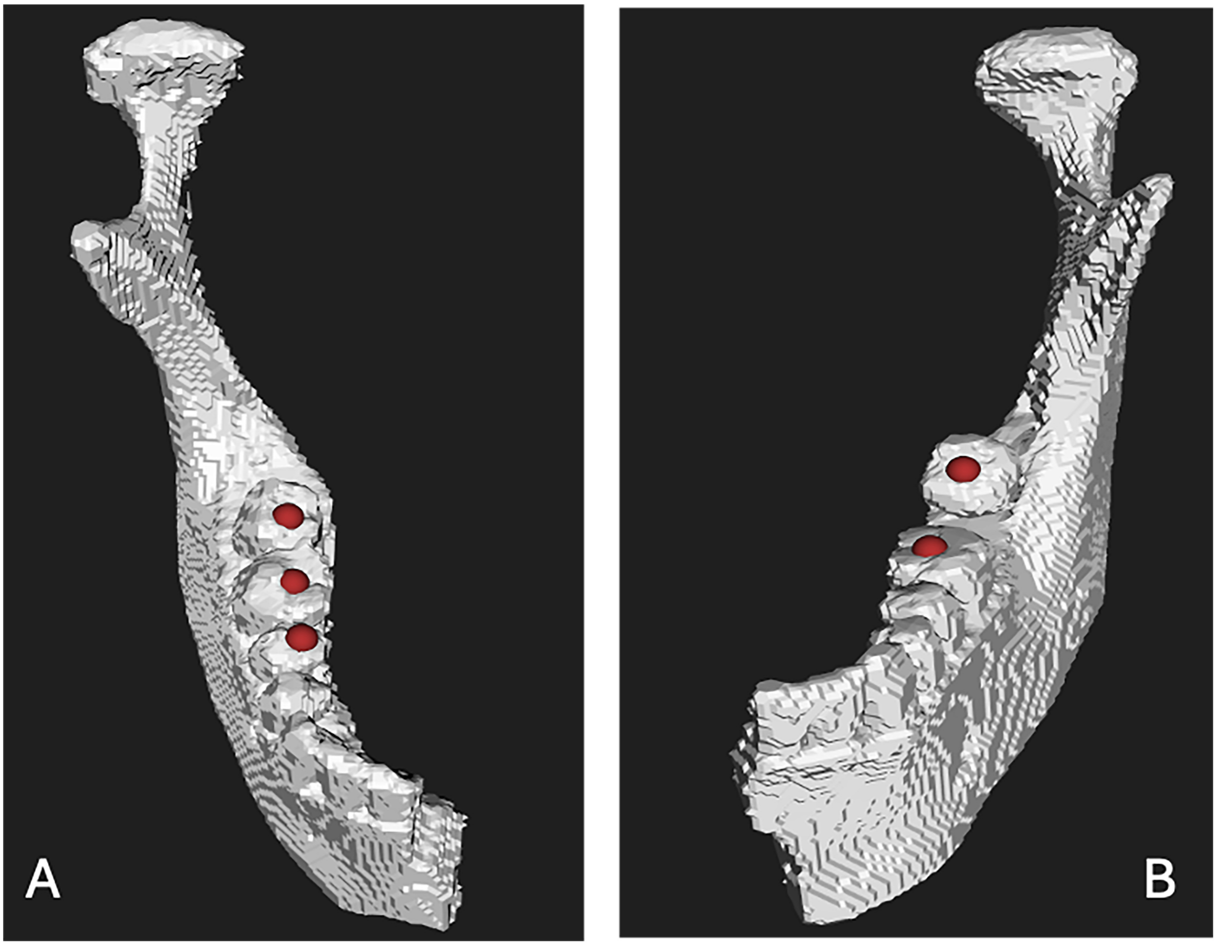

Figure 5. Mandibular dentition with landmark positioning. (A) Lower right dentition with landmarks indicated by red dots; (B) Lower left dentition with landmarks indicated by red dots.

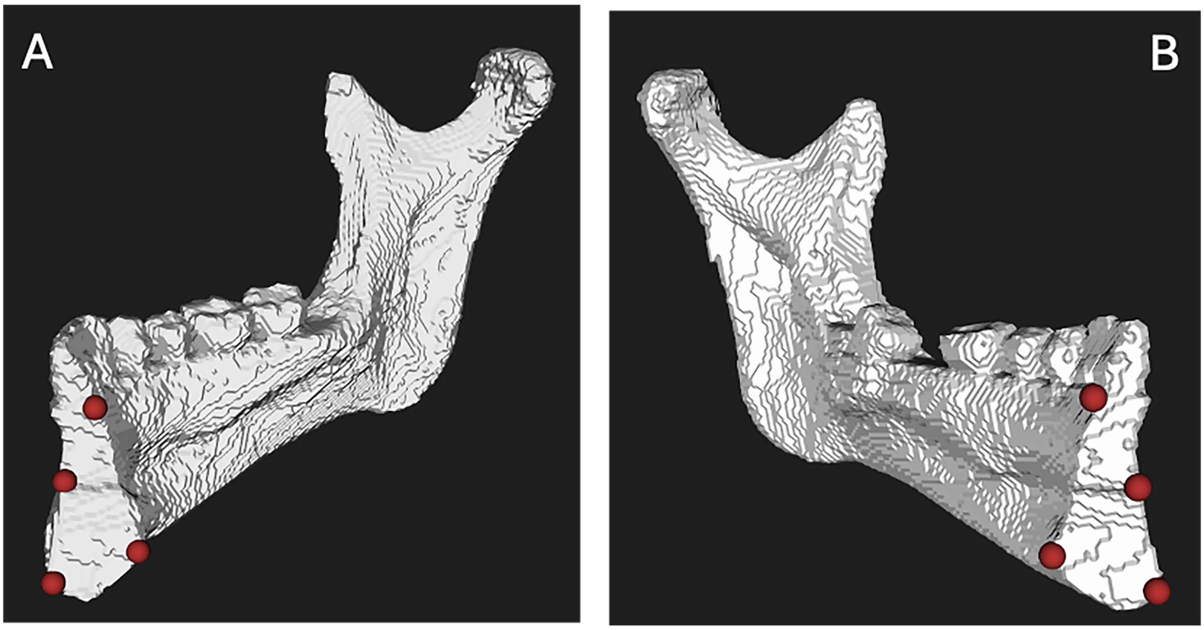

Figure 6. Mandibular fracture landmarks. (A) Right side of the mandible with fracture landmarks indicated by red dots; (B) Left side of the mandible with fracture landmarks indicated by red dots.

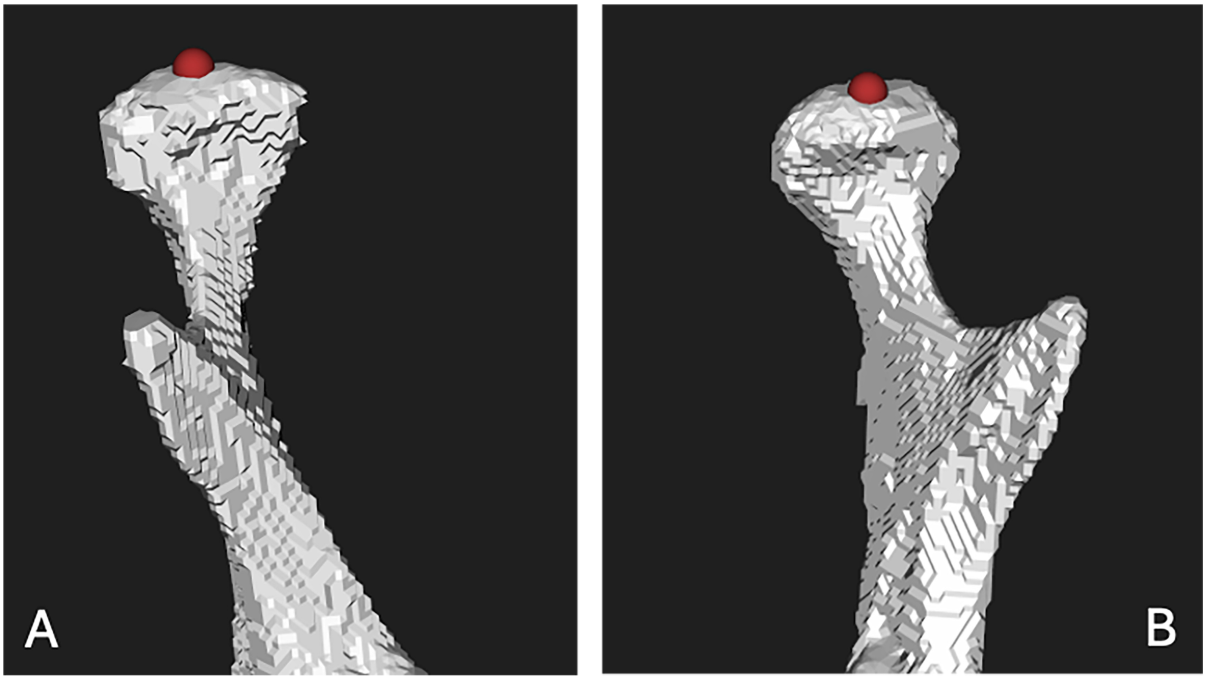

Figure 7. Mandibular condyle head landmarks. (A) Right condyle head of the mandible with a landmark indicated by a red dot; (B) Left condyle head of the mandible with a landmark indicated by a red dot.

Weight assignment in the objective function

Weights for the objective function were determined through 14 experimental iterations by varying weights while maintaining a total sum of 1. The following considerations guided the iterations.

The highest weight is assigned to w6, as aligning the fracture sections is the most fundamental and critical aspect of the surgery. Proper alignment of fracture segments ensures the restoration of the mandible's structural integrity and functional capacity, which are primary objectives in mandibular reconstruction. The smallest weight is assigned to w3, reflecting the clinical observation that patients often do not have perfectly aligned dental midlines prior to fracture. Additionally, in jawbone reduction, aesthetic considerations such as dental midline alignment are of secondary importance compared to functional restoration. Thus, this term is given the lowest priority in the objective function.

Larger weights are assigned to w1 and w2 to minimize the distance between the dental landmarks of the maxilla and mandible. These terms ensure proper dental occlusion, which is essential for functional recovery and patient comfort. The alignment of dental landmarks directly impacts the patient's ability to chew, speak, and maintain oral health.

The weights for the condyle head term (w4 and w5) are assigned to anchor the condyle heads in their target positions. Proper alignment of the condyles is crucial for restoring mandibular articulation and ensuring the stability of the TMJ. These terms contribute to the overall alignment of the mandible by providing a stable reference point for repositioning. The weights w7, w8, and w9 are assigned to mitigate interpenetration and prevent volume overlap among the 3D reconstructed segments. These terms ensure anatomical feasibility and avoid unrealistic configurations that could compromise the surgical outcome and have been given the lowest weights and kept constant along with w3 throughout the experiments.

The experiments are summarized in Table 1. Experiments 7 and 10 are representative cases. In experiment 10, minimizing the distance between the fractures is given the highest priority to determine whether this alone can solve the problem, omitting the occlusion criterion and positioning of the condyle inside the mandibular fossa. Experiment 7 omitted the positioning of the condyle as a factor.

Minimization of the sum of the distances between the fracture landmarks and the dental landmarks to achieve occlusion is the clinical criterion; as such, experiment 13 yields the best performance. The best results are as follows: (i) w6 (fracture alignment) is assigned the highest weight (0.4); (ii) w1 and w2 (dental occlusion) are assigned moderate weights (0.15 each); (iii) w4 and w5 (condylar positioning) are assigned weights of 0.05 each to ensure TMJ stability; (iv) w3 (dental midline alignment) is assigned the lowest weight (0.05); and v) w7, w8, and w9 (interpenetration prevention) are assigned weights of 0.05 each to ensure anatomical feasibility.

Initial alignment results

The mean Euclidean distance for fracture landmarks was 1.39 mm, with additional metrics for dental occlusion (left: 2.53 mm, right: 3.00 mm) and condylar landmarks (left: 2.32 mm, right: 1.79 mm), yielding a combined dental and fracture alignment error (A + B + C) of 6.92 mm.

Fine alignment with ICP

To address overlaps observed between the bone fragments, the SimpleICP - a simplified implementation of the ICP algorithm was employed for precise alignment of fracture fragments. The 3D models of repositioned segments were converted to point clouds, with one designated as the "moving" point cloud and the other as the "fixed" point cloud. The ICP algorithm iteratively minimized discrepancies in the overlap region through the following steps: (i) Matching - correspondences were established between points in the moving and fixed point clouds using a nearest-neighbor search within a threshold defined by the mean Euclidean distance from the GA (1.39 mm), with points lacking correspondences within this threshold being rejected; (ii) Minimization - a point-to-plane error metric was minimized using least-squares optimization to estimate rigid-body transformation parameters (rotation and translation), producing the transformation matrix (H) that aligned the moving point cloud with the fixed one; and (iii) Transformation - the computed transformation matrix was applied to the 3D mesh of the moving segment, and the aligned mesh was exported as an STL file.

Final registration of condylar and dental landmarks

A final rigid registration step was performed to ensure precise alignment of condylar head and dental landmarks [Figure 8]. The source point cloud, comprising condylar head landmarks and the central fossa of mandibular molars, was aligned with the target point cloud, consisting of original condylar landmarks and the mesiopalatal cusp of maxillary molars. A 4 × 4 transformation matrix was computed and applied to the repositioned fragments to ensure accurate TMJ articulation and dental occlusion.

Quantification of the overlap volume and the direct contact area

The quantification of the overlap between two bone fragments can be achieved by computing the volume of their intersecting region. This volume of overlap could serve as a key performance indicator (KPI). A higher overlap volume may signal a false alarm, indicating suboptimal repositioning in which the meshes interpenetrate excessively and deviate from anatomically or mechanically correct alignment.

The fit between repositioned bone fragments can be quantitatively assessed by measuring the direct contact area, which represents the extent of surface adjacency between the fragments following alignment. This metric serves as a KPI for evaluating the effectiveness of the repositioning algorithm, where a higher contact

Table 1. Summary of experiments to determine optimum weights

Exp No.	W1	W2	W4	W5	W6	Fitness	MED fracture (A)	MED occlusion left (B)	MED occlusion right (C)	MED left condyle	MED right condyle	A + B + C
1	0.15	0.15	0.125	0.125	0.25	4.62	1.51	2.85	2.94	0.8	0.6	7.3
2	0.1	0.1	0.15	0.15	0.35	3.91	1.47	3	3	0.54	0.4	7.47
3	0.08	0.08	0.17	0.17	0.3	3.37	1.47	3.02	3.02	0.37	0.31	7.51
4	0.09	0.09	0.16	0.16	0.3	3.59	1.47	3.02	3	0.49	0.37	7.49
5	0.12	0.12	0.1	0.1	0.36	4.37	1.45	2.93	2.99	1	0.61	7.37
6	0.1	0.1	0.1	0.1	0.4	3.99	1.46	2.94	2.99	0.73	0.45	7.39
7	0.15	0.15	0	0	0.5	5.04	1.43	2.16	3.28	10	3.51	6.87
8	0	0	0.15	0.15	0.5	1.65	1.5	4.5	6.37	0.16	0.09	12.37
9	0.16	0.16	0.09	0.09	0.3	4.87	1.45	2.74	2.95	1.09	0.72	7.14
10	0	0	0	0	0.8	2.04	1.43	65.1	44.93	78.07	23.33	111.46
11	0.15	0.15	0.1	0.1	0.3	4.72	1.49	2.82	2.95	0.87	0.68	7.26
12	0.17	0.17	0.08	0.08	0.3	5.04	1.37	2.67	2.95	1.43	1	6.99
13	0.15	0.15	0.05	0.05	0.4	5.11	1.39	2.53	3	2.32	1.79	6.92
14	0.2	0.2	0.05	0.05	0.3	5.2	1.5	2.62	2.87	1.77	1.25	6.99
W3 = W7 = W8 = W9 = 0.05 and kept constant throughout the experiments												

W1, W2 = weights for dental occlusion; W4, W5 = weights for condylar positioning; W6 = weight for fracture alignment; Fitness = overall objective function performance; MED fracture (A) = Mean Euclidean Distance at fracture landmarks; MED occlusion left (B) = Mean Euclidean Distance at left occlusion landmarks; MED occlusion right (C) = Mean Euclidean Distance at right occlusion landmarks; MED left condyle = Mean Euclidean Distance at left condyle landmarks; MED right condyle = Mean Euclidean Distance at right condyle landmarks; A + B + C = combined MED for interfragmentary gap and occlusion accuracy.

area indicates a greater degree of fit, suggesting that the meshes have been repositioned with enhanced accuracy and anatomical fidelity. To establish typical threshold values for this KPI, a statistical analysis of cross-sectional areas from a diverse cohort of healthy mandibles and varied fracture line morphologies is recommended, enabling the identification of benchmarks that correlate with successful repositioning outcomes.

The overlap volume and contact area were computed in Python using the trimesh library (version 4.5.2), with Boolean mesh intersection performed via the Manifold3d backend. The fracture fragments were loaded as individual STL meshes following the GA-based optimization and ICP registration steps. Pairwise Boolean intersections were computed between the adjacent fragments. All input meshes were confirmed to be watertight (manifold, closed surfaces) prior to the Boolean operation, satisfying the precondition required for valid volume computation via the Divergence Theorem.

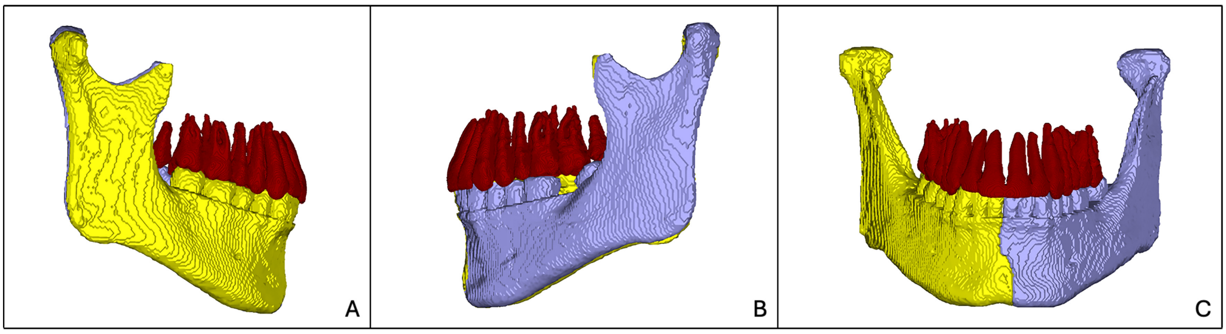

Figure 8. Final registration of condylar and dental landmarks in the simulated fracture. (A) Right lateral view of the mandible with dentition; (B) Left lateral view of the mandible with dentition; (C) Frontal view showing the complete mandibular arch and dentition after rigid registration of condylar head and dental landmarks.

The overlap volume in the repositioned simulated fracture was 167.50 mm^3 and the corresponding direct contact area was 754.44 mm^2.

Algorithm performance

The synthetic validation model provided a controlled environment for quantitative analysis, allowing a direct comparison between the algorithmically reduced and the original unfractured mandible geometry. An illustrative clinical application was subsequently performed on three mandible fracture cases to demonstrate the algorithm's technical feasibility across varying fracture patterns and degrees of displacement. Computation time for each reduction averaged 25-28 min on a standard workstation (Intel Core i7, 32 GB RAM). The algorithm showed robust convergence behavior and stable accuracy across all tested fracture configurations.

RESULTS

Surface distance analysis

To evaluate the accuracy of the proposed repositioning algorithm, the repositioned 3D mandibular model was superimposed onto the original pre-fracture model. A surface distance map was generated with the Python library PyVista (version 0.44.1)[40] to quantify spatial discrepancies between the repositioned and original configurations, providing both visual and numerical assessments of anatomical alignment. The maximum deviation between the repositioned model and the pre-fracture reference was 1.58 mm, with minimum deviations approaching 0 mm. Notably, deviations along the fracture cut surfaces were predominantly within 1 mm, aligning with the acceptable interfragmentary gap for ORIF as reported in the literature[26]. These results indicate that the algorithm achieves high anatomical accuracy, particularly in regions critical for fracture alignment and bone healing [Figure 9].

Occlusal alignment evaluation

The quality of dental occlusion was assessed by measuring the Euclidean distance between the mesiopalatal cusp of the maxillary molars and the central groove of the mandibular molars, comparing the pre-fracture and repositioned models. Table 2 summarizes the molar relationship metrics for both sides of the mandible. The deviations in molar relations were minimal, with 0.07 mm on the right side and 0.15 mm on the left side. These results demonstrate that the repositioning algorithm successfully restored occlusal relationships comparable to the pre-fracture state, ensuring functional bite mechanics and supporting the structural integrity of the mandibular fracture reduction.

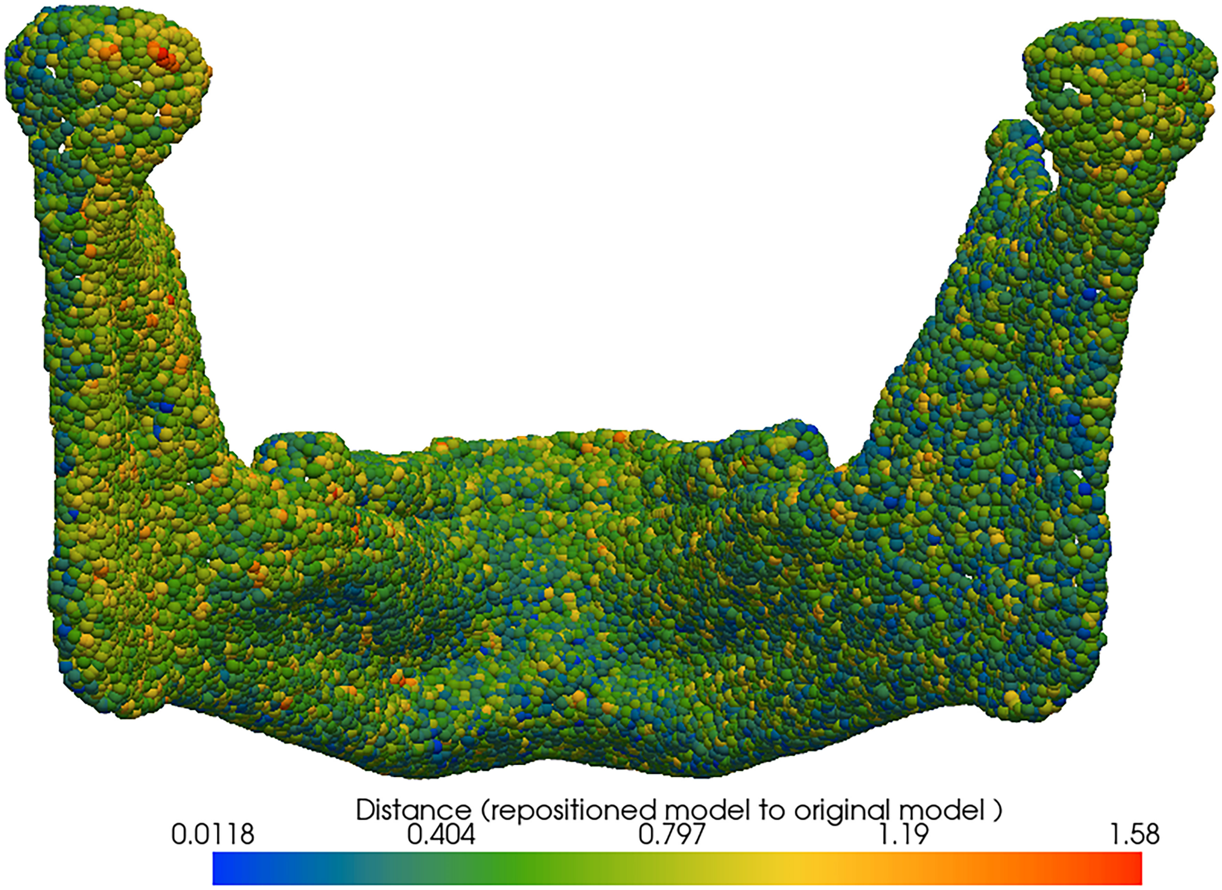

Figure 9. Surface-distance map; repositioned model to original model.

Table 2. Evaluation of deviation in right and left molar relation based on occlusion

Molar relation	Original model	Repositioned model	Deviation
Right molar relation (R)	1.55 mm	1.62	0.07 mm
Left molar relation (L)	3.90 mm	3.75	0.15 mm

Application to Clinical Cases

The algorithm was applied to three clinical cases to evaluate its feasibility. Specifications of the fractures are as follows:

Case 1

This is a clinical case involving a single fracture line in the angular region of the mandible. The fracture resulted in significant displacement of the bone fragments prior to repositioning [Figure 10A]. Due to the patient's dentition, only one corresponding dental landmark was available for algorithmic alignment, as posterior molars required for additional occlusal reference points were absent. Four corresponding fracture landmarks were identified in the mandibular fracture region. Supplementary reference points included the midpoints of the maxillary and mandibular arches as well as anatomical landmarks on the condylar head. The repositioned model is shown in Figure 10B.

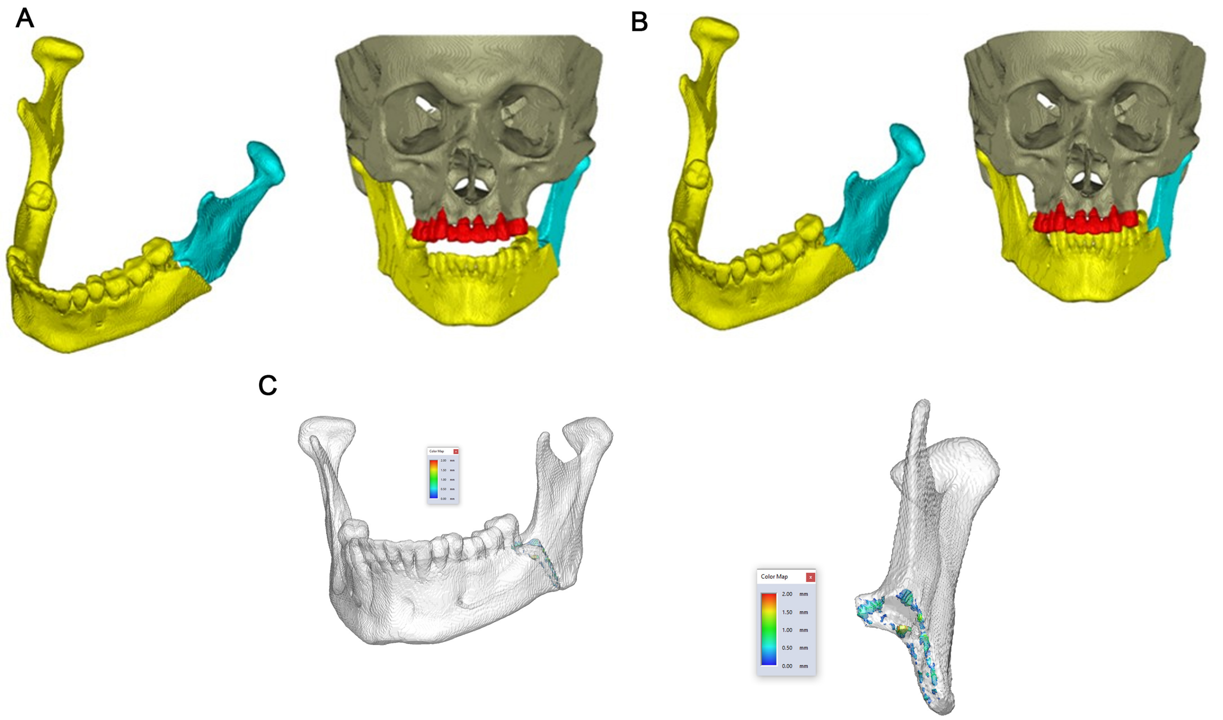

Figure 10. Virtual fracture reduction for Case 1. (A) Pre-reduction view showing displaced fragments; (B) Post-reduction configuration following algorithmic alignment; (C) Color-coded overlap map illustrating the congruence of fracture interfaces.

Case 2

In Case 2, two fracture lines were present: one located in the left mandibular angle and another in the right mandibular body region. Three-dimensional reconstruction from CT data revealed significant displacement of the fracture fragments [Figure 11A]. For alignment, two corresponding molar landmarks were identified bilaterally in the mandibular and maxillary structures. Additionally, anatomical landmarks on the condyle heads and four pairs of fracture-specific landmarks were selected to support repositioning. The repositioned model is given in Figure 11B.

Case 3

Case 3 presented with two fracture lines, both located within the mandibular body region. The first fracture was identified at the third molar on the left side, while the second was situated at the first molar on the right side [Figure 12A]. For repositioning, four pairs of corresponding dental landmarks were used in combination with nine pairs of fracture-specific landmarks to ensure both occlusal and structural accuracy. The repositioned model is given in Figure 12B.

Clinical evaluation of the VFR algorithm

Objective evaluation of fracture repositioning in clinical cases presents inherent challenges, as no pre-fracture reference model exists for comparison. To address this limitation, several corresponding anatomical landmarks were placed on the repositioned bone segments. The mean Euclidean distance between these landmarks was calculated for each fracture. The resultant values ranged from 0.22 to 0.70 mm across the five fracture segments in the three cases, with an overall mean of 0.50 ± 0.19 mm (95%CI: 0.27-0.74 mm), indicating consistent alignment. This value lies well within the clinically acceptable threshold of 1 mm, thereby indicating accurate repositioning. The results are summarized in Table 3.

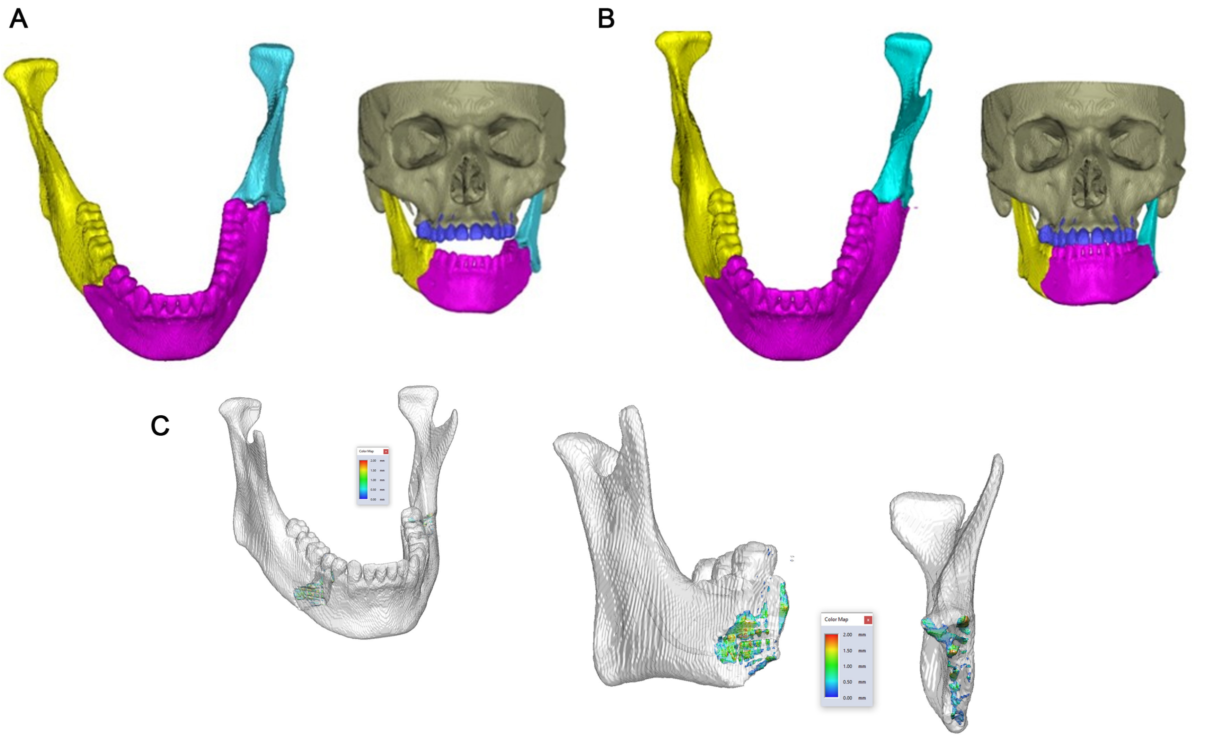

Figure 11. Virtual fracture reduction for Case 2. (A) Pre-reduction view showing displaced fragments; (B) Post-reduction configuration following algorithmic alignment; (C) Color-coded overlap map illustrating the congruence of fracture interfaces.

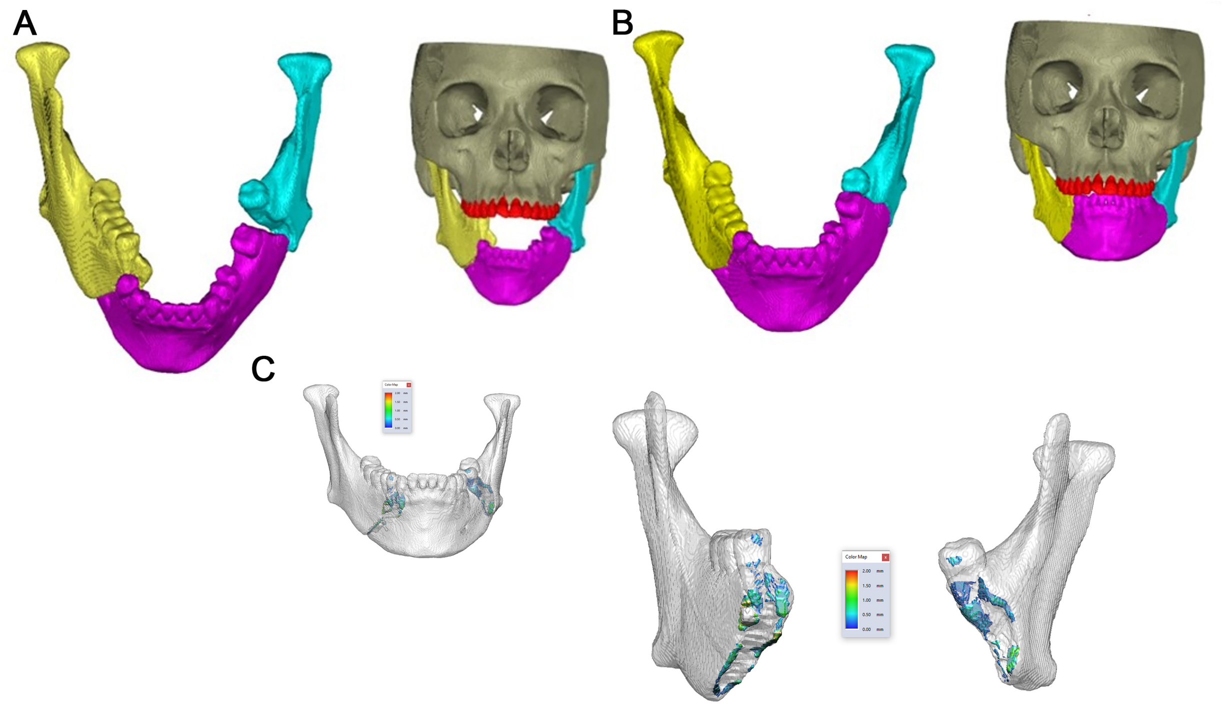

Figure 12. Virtual fracture reduction for Case 3. (A) Pre-reduction view showing displaced fragments; (B) Post-reduction configuration following algorithmic alignment; (C) Color-coded overlap map illustrating the congruence of fracture interfaces.

Table 3. Mean Euclidean distance (mm) of virtual fracture reduction per fracture segment across clinical cases, with overall mean, standard deviation, and 95%CI

Case	Mean Euclidean distance (mm)
Case 1	0.60
Case 2 (Left)	0.43
Case 2 (Right)	0.70
Case 3 (Left)	0.22
Case 3 (Right)	0.57
Mean ± SD	0.50 ± 0.19
95% CI	0.27-0.74

CI: Confidence interval; SD: standard deviation.

Table 4. Case 1, Case 2 and Case 3 quantitative KPIs are summarized

KPI	Case 1	Case 2	Case 3
Overlap Volume (Left)	28.54 mm^3	61.86 mm^3	50.67 mm^3
Direct Contact Area (Left)	216.00 mm^2	338.65 mm^2	405.68 mm^2
Overlap Volume (Right)	N/A	119.26 mm^3	113.47 mm^3
Direct Contact Area (Right)	N/A	530.07 mm^2	533.17 mm^2

KPI: Key performance indicator; VFR: virtual fracture reduction; MED: mean Euclidean distance. N/A indicates that the specific metric was not applicable to the anatomical features of the case.

Table 5. Algorithm runtime for the clinical cases

Case	Algorithm runtime (in minutes)
Case 1	25.3
Case 2	27.6
Case 3	26.8

To further analyze repositioning accuracy, the fracture segments were examined for potential overlaps. A color-coded intersection colormap was generated using Geomagic Freeform 2024 software (v2024.0.87, Oqton Inc.) to visualize the degree of congruence along the fracture contours [Figures 10C, 11C and 12C]. Overlaps within a 2 mm threshold were plotted, revealing that most outer contours showed high congruence, with deviations typically ranging between 0.60 and 1.00 mm. The KPIs for each case were calculated as described in section 2.10 and summarized in Table 4. The algorithm runtime for each case is given in Table 5.

DISCUSSION

VFR represents an emerging technique to streamline preoperative surgical planning and catalyze fast-track fracture repair. In this study, we developed and tested a novel algorithm that showed high precision in mandibular fracture reduction, closely restoring pre-fracture anatomy.

In our study, the repositioned mandible segments aligned with high accuracy. The quantified surface deviations (mostly < 1 mm) are comparable to recent digital-reduction models that reported similarly close realignment[41]. For instance, Nilsson *et al.* performed VFR in 12 patients and found interfragmentary distances of less than 2 mm[26]. In parallel with this finding, Saloniemi *et al.* included 10 patients with dislocated subcondylar mandibular fractures. The authors reported close alignment of fracture lines (< 2 mm)[42]. Such close fracture reduction may support direct lamellar bone healing[43-45]. Overall, the algorithm may serve as a virtual tool to closely restore pre-injury anatomy.

The algorithm further showed promising occlusal relationship reconstruction, achieving molar relationships similar to the preoperative state (within 0.1 mm). This finding mirrors previous research by Wang *et al*., who performed CT-based VFR planning for 27 patients with fractures. Interestingly, the authors reported the restoration of the original occlusion with less than 0.5 mm deviation[46]. Similarly, a 2024 Chinese study enrolled 15 patients with old mandible fractures who presented with postoperative malocclusion defects. Leveraging VFR, occlusal function reconstruction was achieved in all cases[47]. Such precise occlusal alignment is crucial for functional bite mechanics and positive long-term outcomes[48]. Collectively, our study presents an algorithm to support surgeons in restoring the patient's pre-fracture occlusion without extensive intraoperative gauging, potentially reducing postoperative malocclusion and the need for secondary revisions.

In the three representative cases (simple and comminuted fractures), mean interfragmentary gaps were 0.22-0.70 mm. Although a direct pre-trauma comparison was unavailable, the sub-millimeter deviations were comparable to the typical precision of manual reduction[12,49-51]. This consistency across different fracture patterns suggests robustness of the method. Clinically, these results imply that the algorithm could standardize reduction even in complex bilateral or dislocated fractures, providing surgeons with a quantitative target for fragment positioning and reducing reliance on subjective alignment or interdental fixation. The KPIs developed herein provide a more comprehensive evaluation framework, moving beyond simplistic metrics such as Euclidean distance between fracture surfaces and thereby adding robustness to the assessment methodology. Nevertheless, the clinical applicability of the proposed KPIs warrants further statistical modeling and rigorous validation prior to their adoption as reliable performance metrics. Normative values for contact areas and overlapping volumes across distinct anatomical regions should be established through studies that include larger, more diverse datasets. It is important to address the variation observed in KPIs, such as overlap volumes, which ranged from 28.54 to 119.26 mm^3. These variations represent a direct consequence of patient-specific anatomical limitations rather than unexplained algorithmic errors. For instance, in Case 1, the absence of posterior molars limited the availability of occlusal reference points, resulting in greater volume overlap compared to fully dentate cases. This highlights a current technical boundary in applying the algorithm to partially edentulous patients, where landmark sparsity directly influences the algorithmic fit. However, future studies are warranted to apply this algorithm to larger patient populations with challenging mandibular fractures or revision surgery.

Despite its promise, VFR is not without challenges. CT artefacts, slice thickness, and segmentation errors can distort the STL geometry and fracture line definition. Landmark identification is another critical source of error, particularly in comminuted or edentulous areas where reliable reference points are scarce. Condylar positioning remains difficult to standardize virtually, and even small rotational mismatches may translate into altered TMJ loading[52,53]. Algorithm optimization in surgical fields can also be fragile - different weight settings or local minima may yield reductions that appear correct but are not anatomically optimal[54,55]. Translating the virtual plan into the operating room adds another layer of complexity, as 3D-printed guides or pre-bent plates may introduce millimetric discrepancies through printing tolerances, sterilization warping, or screw placement. In addition, workflow demands - software licensing, segmentation time, and technical expertise - limit routine clinical use, while chronic or old fractures with callus formation or tooth migration present alignment targets that are more difficult to define[27,56,57]. Finally, many studies emphasize bone-level accuracy, with less evidence on long-term outcomes such as masticatory function, TMJ health, or neurosensory recovery.

Overall, for clinicians, these results highlight that VFR has the potential to augment mandibular fracture management with millimetric precision, particularly in complex or bilateral injuries. At present, however, physicians should view VFR as a supportive tool rather than a replacement for intraoperative judgment, especially in cases complicated by callus formation, poor imaging quality, or edentulism. Patients, meanwhile, should be counseled that while digital planning may improve anatomical alignment and shorten operating time, robust data on functional recovery, TMJ outcomes, and long-term complication rates remain limited. Future research should prioritize larger prospective studies to compare VFR with conventional reduction across diverse fracture types, as well as multicenter trials to evaluate reproducibility in real-world trauma workflows. Moreover, cost-effectiveness analyses and integration into fast-track trauma care pathways are needed to determine clinical feasibility at scale. Ultimately, VFR represents a promising adjunct in maxillofacial trauma surgery, but its broader adoption will require validation beyond geometric accuracy to encompass functional, economic, and patient-reported outcomes.

LIMITATIONS

This study has several limitations, primarily because it is a preliminary technical report rather than a comprehensive clinical trial. First, the clinical evaluation was limited to three illustrative cases without formal statistical analysis; thus, the findings serve as an algorithmic proof of concept rather than broad clinical validation. In these clinical cases, no true pre-fracture reference was available, so accuracy was inferred from surrogate landmarks and surface maps.

Importantly, the proposed method is strictly landmark-dependent. Algorithm performance and fit can be significantly affected by anatomical limitations, including partial edentulism, comminution, callus, or CT artifacts. For instance, the wide variation observed in overlap volumes within our KPIs (ranging from 28.54 to 119.26 mm^3) is directly attributable to anatomical variations like missing posterior molars (as seen in Case 1), which reduce the availability of occlusal reference points, rather than unexplained algorithmic errors.

Furthermore, soft-tissue forces, condylar seating, and TMJ loading were not modeled, and the algorithm relies on weight tuning that may not generalize beyond this dataset. Translation into the operating room (OR) introduces additional errors due to guide fabrication, sterilization, and screw placement, none of which were systematically tested. Planning time, learning curve, and cost implications were also not evaluated. Finally, outcomes were limited to bone geometry, without functional or patient-reported measures, and reproducibility across operators or centers was not assessed.

Future work should include larger, multicenter cohorts powered for robust statistical analysis to definitively validate clinical efficacy. Such studies should incorporate standardized functional outcomes, error-budget assessments spanning imaging to fixation, robustness testing of algorithm parameters across diverse anatomies, and evaluations of workflow efficiency and cost-effectiveness. Integration with intraoperative navigation, splinting, and automated landmarking may further enhance reliability and clinical adoption.

CONCLUSIONS

The proposed VFR algorithm reliably restores preoperative mandibular anatomy and occlusion with high accuracy in all applied clinical cases. Its precision matches clinically accepted reduction tolerances and could improve ORIF outcomes by providing surgeons precise realignment targets and rapid reconstruction strategies. Further clinical validation and larger-scale trials are warranted to assess its long-term impact on surgical efficiency and fracture healing.

DECLARATIONS

Acknowledgments

Figure 1 (Overview of the VFR algorithm) was created using Microsoft PowerPoint (Version 2607, Build 16.0.20228.20124). Visualizations of the synthetic mandible model and simulated fracture [Figures 2 and 3] were generated using Materialise Mimics 23.0 (Materialise NV, Leuven, Belgium). Landmarks were positioned and visualized using the developed Landmark Editor [Figures 4-8]. The repositioned simulated

fracture was visualized in Materialise Mimics. The surface distance map [Figure 9] was generated using the Python library PyVista (version 0.44.1). Pre-reduction and post-reduction views were obtained using Materialise Mimics [Figures 10A, 10B, 11A, 11B, 12A and 12B]. Color-coded intersection maps for the repositioned clinical cases were generated using Geomagic Freeform 2024 (v2024.0.87, Oqton Inc.) [Figures 10C, 11C and 12C]. All figures are screenshots.

Authors' contributions

Conceptualized and developed the virtual fracture reduction algorithm, implemented the two-stage computational pipeline, performed formal analysis and validation, and co-drafted the original manuscript: Scariah A

Preparation and review of the manuscript and co-drafted it: Knoedler L

Algorithm validation and verification and supervised the master's thesis: Koett T

Clinical data collection, project administration, and funding acquisition: Aksu A

Algorithm design, study methodology, validation and verification, and provided primary supervision of the study: Potrusil T

Project administration and funding acquisition, provided oversight of the research work, and contributed to manuscript review: Niederegger T

Provided oversight of the research work and contributed to manuscript review: Satea M

Algorithm design and study conceptualization and provided supervision of the study: Fischer J

Provided resources, including equipment and patient access, and contributed to manuscript review: Heiland M

Study conceptualization and research design, clinical data collection and case provision, and overall supervision of the research work: Voss JO

All authors have read and approved the final version of the manuscript.

Availability of data and materials

The medical imaging data and generated 3D models used in the present study are not publicly available. All datasets are derived from retrospective, patient-related clinical CT imaging data obtained as part of routine preoperative assessment in patients with mandibular fractures and are subject to institutional, ethical, and data-protection restrictions (GDPR).

Anonymized preoperative DICOM CT datasets from 88 individuals were used for the development of the presented Virtual Fracture Reduction algorithm. The necessary segmentations, 3D surface models, anatomical landmarks, and STL files were generated during the study.

Anonymized imaging data, derived 3D models and data as mentioned, as well as surgery planning data that support the findings of this study, may be made available from the corresponding author upon reasonable request. Requests are subject to approval by the responsible institutional bodies, compliance with the ethics approval granted by the Ethics Committee at Charité - Universitätsmedizin Berlin (EA2/214/24), compliance with applicable data protection regulations (including the EU General Data Protection Regulation), and execution of an appropriate data use agreement.

Materials that do not compromise patient privacy, including algorithmic descriptions, parameter settings, and landmark definitions, are described in the Methods section and may be made available upon reasonable request.

AI and AI-assisted tools statement

Not applicable

Financial support and sponsorship

None.

Conflicts of interest

Heiland M, MD, DMD, received a speaker honorarium and research funding from KLS Martin SE & Co. KG. Scariah A, MSc, Koett T, BSc, and Aksu A, MSc are employees of KLS Martin SE & Co. KG; Potrusil T is an employee of CADS GmbH. The other authors have no conflicts of interest to declare.

Ethical approval and consent to participate

Ethical approval for this retrospective study was granted by the Ethics Committee of Charité - Universitätsmedizin Berlin (approval number: EA2/214/24). The requirement for individual informed consent was waived due to the retrospective design and complete anonymization of patient data. No personally identifiable information is presented in this manuscript.

Consent for publication

Not applicable.

Copyright

REFERENCES

1. Zhang ZX, Xie L, Li Z. Global, regional, and national burdens of facial fractures: a systematic analysis of the global burden of Disease 2019. *BMC Oral Health*. 2024;24:282. DOI PubMed PMC
2. Chen H, Jia Z, He X, Feng X, Wu M, Zhang S. Burden and trends of facial fractures in China and the United States based on GBD 2021 analysis. *Sci Rep*. 2025;15:8328. DOI PubMed PMC
3. Adik K, Lamb P, Moran M, Childs D, Francis A, Vinyard CJ. Trends in mandibular fractures in the USA: a 20-year retrospective analysis. *Dent Traumatol*. 2023;39:425-36. DOI PubMed
4. Afrooz PN, Bykowski MR, James IB, Daniali LN, Clavijo-Alvarez JA. The Epidemiology of Mandibular Fractures in the United States, Part 1: A Review of 13,142 Cases from the US National Trauma Data Bank. *J Oral Maxillofac Surg*. 2015;73:2361-6. DOI PubMed
5. Døving M, Næss I, Galteland P, et al. Anatomical distribution of mandibular fractures from severe bicycling accidents: a 12-year experience from a Norwegian level 1 trauma center. *Dent Traumatol*. 2022;38:424-30. DOI PubMed PMC
6. Uppada UK, Sinha R, Susmitha M, Praseedha B, Kiran BR. Mandibular fracture patterns in a rural setup: a 7-year retrospective study. *J Maxillofac Oral Surg*. 2022;21:1349-54. DOI PubMed PMC
7. Ellis E, Moos KF, el-Attar A. Ten years of mandibular fractures: an analysis of 2,137 cases. *Oral Surg Oral Med Oral Pathol*. 1985;59:120-9. DOI PubMed
8. Buch K, Mottalib A, Nadgir RN, et al. , Unifocal versus multifocal mandibular fractures and injury location. *Emerg Radiol*. 2016;23:161-7. DOI PubMed
9. Weitzman RE, Subramanian T, Zhao K, Shomorony A, Sclafani AP. Trends in management and cost burden of facial fractures: a 14-year analysis. *Laryngoscope*. 2024;134:3120-6. DOI PubMed
10. Wu Y, Long X, Fang W, et al. Management of paediatric mandibular condylar fractures with screw-based semi-rigid intermaxillary fixation. *Int J Oral Maxillofac Surg*. 2012;41:55-60. DOI PubMed
11. Carlson AR, Shammas RL, Allori AC, Powers DB. A technique for reduction of edentulous fractures using dentures and SMARTLock hybrid fixation system. *Plast Reconstr Surg Glob Open*. 2017;5:e1473. DOI PubMed PMC
12. Sobrero F, Roccia F, Omedè M, et al. Current strategies for treatment of mandibular fractures with plate osteosynthesis: a European prospective study. *J Craniofac Surg*. 2024;35:1120-4. DOI PubMed
13. Seol GJ, Jeon EG, Lee JS, et al. Reconstruction plates used in the surgery for mandibular discontinuity defect. *J Korean Assoc Oral Maxillofac Surg*. 2014;40:266-71. DOI PubMed PMC
14. Christensen BJ, Mercante DE, Neary JP, King BJ. Risk factors for severe complications of operative mandibular fractures. *J Oral Maxillofac Surg*. 2017;75:787.e1-8. DOI PubMed
15. Lamphier J, Ziccardi V, Ruvo A, Janel M. Complications of mandibular fractures in an urban teaching center. *J Oral Maxillofac Surg*. 2003;61:745-9. DOI PubMed
16. Steffen C, Welter M, Fischer H, et al. Revision surgery with refixation after mandibular fractures. *Craniomaxillofac Trauma Reconstr*. 2024;17:214-24. DOI PubMed PMC
17. Barr ML, Haveles CS, Rezzadeh KS, et al. Virtual surgical planning for mandibular reconstruction with the fibula free flap: a systematic review and meta-analysis. *Ann Plast Surg*. 2020;84:117-22. DOI PubMed

18. Stokbro K, Aagaard E, Torkov P, Bell RB, Thygesen T. Virtual planning in orthognathic surgery. *Int J Oral Maxillofac Surg.* 2014;43:957-65. DOI PubMed
19. Hanken H, Schablowsky C, Smeets R, et al. Virtual planning of complex head and neck reconstruction results in satisfactory match between real outcomes and virtual models. *Clin Oral Investig.* 2015;19:647-56. DOI PubMed
20. Ebker T, Korn P, Heiland M, Bumann A. Comprehensive virtual orthognathic planning concept in surgery-first patients. *Br J Oral Maxillofac Surg.* 2022;60:1092-6. DOI PubMed
21. Voss JO, Varjas V, Raguse JD, Thieme N, Richards RG, Kamer L. Computed tomography-based virtual fracture reduction techniques in bimandibular fractures. *J Craniomaxillofac Surg.* 2016;44:177-85. DOI PubMed
22. Troise S, De Fazio GR, Committeri U, et al. Mandibular reconstruction after post-traumatic complex fracture: Comparison analysis between traditional and virtually planned surgery. *J Stomatol Oral Maxillofac Surg.* 2025;126:102029. DOI PubMed
23. Pucci R, Weyh A, Smotherman C, Valentini V, Bunnell A, Fernandes R. Accuracy of virtual planned surgery versus conventional free-hand surgery for reconstruction of the mandible with osteocutaneous free flaps. *Int J Oral Maxillofac Surg.* 2020;49:1153-61. DOI PubMed
24. Singerman KW, Morisada MV, Kriet JD, Flynn JP, Humphrey CD. Virtual surgical planning for management of acute maxillofacial trauma. *Craniomaxillofac Trauma Reconstr.* 2025;18:18. DOI PubMed PMC
25. Shakya S, Li KD, Huang D, Liu ZQ, Zhang X, Liu L. Virtual surgical planning is a useful tool in the surgical management of mandibular condylar fractures. *Chin J Traumatol.* 2022;25:151-5. DOI PubMed PMC
26. Nilsson J, Nysjö F, Nyström I, Kämpe J, Thor A. Evaluation of in-house, haptic assisted surgical planning for virtual reduction of complex mandibular fractures. *Int J Comput Assist Radiol Surg.* 2021;16:1059-68. DOI PubMed PMC
27. Moolenaar JZ, Tümer N, Checa S. Computer-assisted preoperative planning of bone fracture fixation surgery: a state-of-the-art review. *Front Bioeng Biotechnol.* 2022;10:1037048. DOI PubMed PMC
28. Minnema J, Ernst A, van Eijnatten M, et al. A review on the application of deep learning for CT reconstruction, bone segmentation and surgical planning in oral and maxillofacial surgery. *Dentomaxillofac Radiol.* 2022;51:20210437. DOI PubMed PMC
29. Schvartzman SC, Silva R, Salisbury K, Gaudilliere D, Girod S. Computer-aided trauma simulation system with haptic feedback is easy and fast for oral-maxillofacial surgeons to learn and use. *J Oral Maxillofac Surg.* 2014;72:1984-93. DOI PubMed
30. Jiménez-Delgado JJ, Paulano-Godino F, Pulidoram-Ramírez R, Jiménez-Pérez JR. Computer assisted preoperative planning of bone fracture reduction: simulation techniques and new trends. *Med Image Anal.* 2016;30:30-45. DOI PubMed
31. Casari FA, Roner S, Fürnstahl P, Nagy L, Schweizer A. Computer-assisted open reduction internal fixation of intraarticular radius fractures navigated with patient-specific instrumentation, a prospective case series. *Arch Orthop Trauma Surg.* 2021;141:1425-32. DOI PubMed PMC
32. Zeng B, Wang H, Tao X, Shi H, Joskowicz L, Chen X. A bidirectional framework for fracture simulation and deformation-based restoration prediction in pelvic fracture surgical planning. *Med Image Anal.* 2024;97:103267. DOI PubMed
33. Okada T, Iwasaki Y, Koyama T, et al. Computer-assisted preoperative planning for reduction of proximal femoral fracture using 3-D-CT data. *IEEE Trans Biomed Eng.* 2009;56:749-59. DOI PubMed
34. Han R, Uneri A, Vijayan RC, et al. Fracture reduction planning and guidance in orthopaedic trauma surgery via multi-body image registration. *Med Image Anal.* 2021;68:101917. DOI PubMed PMC
35. Ead MS, Palizi M, Jaremko JL, Westover L, Duke KK. Development and application of the average pelvic shape in virtual pelvic fracture reconstruction. *Int J Med Robot.* 2021;17:e2199. DOI PubMed
36. Sharaf BA, Morris JM, Kuruoglu D. EPPOCRATIS: a point-of-care utilization of virtual surgical planning and three-dimensional printing for the management of acute craniomaxillofacial trauma. *J Clin Med.* 2021;10:5640. DOI PubMed PMC
37. Besl PJ, McKay ND. A method for registration of 3-D shapes. *IEEE Trans Pattern Anal Mach Intell.* 1992;14:239-56. DOI
38. Pankert T, Lee H, Peters F, Hölzle F, Modabber A, Raith S. Mandible segmentation from CT data for virtual surgical planning using an augmented two-stepped convolutional neural network. *Int J Comput Assist Radiol Surg.* 2023;18:1479-88. DOI PubMed PMC
39. Fortin FA, De Rainville FM, Gardner MA, Parizeau M, Gagné. DEAP: evolutionary algorithms made easy. *J Mach Learn Res.* 2012;13:2171-5. Available from: https://jmlr.org/papers/v13/fortin12a.html. [Last accessed on 17 Aug 2026].
40. Sullivan C, Kaszynski A. PyVista: 3D plotting and mesh analysis through a streamlined interface for the Visualization Toolkit (VTK). *J Open Source Softw.* 2019;4:1450. DOI
41. Kim J, Jeung D, Cho R, Yang B, Hong J. A proof of concept: optimized jawbone-reduction model for mandibular fracture surgery. *J Imaging Inform Med.* 2024;37:1151-9. DOI PubMed PMC
42. Saloniemi M, Salli M, Lehtinen V, Snäll J. Primary surgery of subcondylar mandibular fracture using patient-specific implant: the Helsinki protocol. *Oral Maxillofac Surg.* 2025;29:46. DOI PubMed PMC
43. Einhorn TA, Gerstenfeld LC. Fracture healing: mechanisms and interventions. *Nat Rev Rheumatol.* 2015;11:45-54. DOI PubMed PMC
44. Burgan J, Rahmati M, Lee M, Saiz AM. Innate immune response to bone fracture healing. *Bone.* 2025;190:117327. DOI PubMed

45. Kim SY, Choi YH, Kim YK. Postoperative malocclusion after maxillofacial fracture management: a retrospective case study. *Maxillofac Plast Reconstr Surg.* 2018;40:27. DOI PubMed PMC
46. Wang H, Chi Y, Hu Y, et al. Accuracy analysis of the digital occlusal relationship reconstruction workflow in patients with maxillofacial fractures: an in vitro retrospective cohort study. *J Dent.* 2025;154:105590. DOI PubMed
47. Ding MC, Jing BY, Shi J, et al. A retrospective study of occlusal reconstruction in patients with old jaw fractures and dentition defects. *Chin J Traumatol.* 2024;27:272-8. DOI PubMed PMC
48. Perez D, Ellis E 3rd. Complications of mandibular fracture repair and secondary reconstruction. *Semin Plast Surg.* 2020;34:225-31. DOI PubMed PMC
49. Sobrero F, Roccia F, Vilaplana V, et al. Manual versus rigid intraoperative maxillo-mandibular fixation in the surgical management of mandibular fractures: a European prospective analysis. *Dent Traumatol.* 2023;39:448-54. DOI PubMed
50. Batbayar EO, Malwand S, Dijkstra PU, Bos RRM, van Minnen B. Accuracy and outcome of mandibular fracture reduction without and with an aid of a repositioning forceps. *Oral Maxillofac Surg.* 2019;23:201-8. DOI PubMed PMC
51. Gruber LJ, Egger J, Bönsch A, et al. Accuracy and precision of mandible segmentation and its clinical implications: virtual reality, desktop screen and artificial intelligence. *Expert Syst Appl.* 2024;239:122275. DOI
52. Holte MB, Pinholt EM. Validation of a fully automatic three-dimensional assessment of orthognathic surgery. *J Craniomaxillofac Surg.* 2024;52:438-46. DOI PubMed
53. Kim SR, Jang S, Ahn KM, Lee JH. Evaluation of effective condyle positioning assisted by 3D surgical guide in mandibular reconstruction using osteocutaneous free flap. *Materials.* 2020;13:2333. DOI PubMed PMC
54. Mithany RH, Aslam S, Abdallah S, et al. Advancements and challenges in the application of artificial intelligence in surgical arena: a literature review. *Cureus.* 2023;15;e47924. DOI PubMed PMC
55. Adegbesan A, Akingbola A, Aremu O, Adewole O, Amamdikwa JC, Shagaya U. From scalpels to algorithms: the risk of dependence on artificial intelligence in surgery. *J Med Surg Public Health.* 2024;3:100140. DOI
56. Yazigi C, Chaar MS, Busch R, Kern M. The effect of sterilization on the accuracy and fit of 3D-printed surgical guides. *Materials.* 2023;16:5305. DOI PubMed PMC
57. Popescu D, Iacob MC, Marinescu R. Dimensional accuracy of 3D-printed surgical cutting guides after hospital sterilization: a comparative evaluation of ten MEX materials. *3D Print Med.* 2025;11:44. DOI PubMed PMC